INSTITUTE OF PHYSICS PUBLISHING JOURNAL OF PHYSICS D: APPLIED PHYSICS

J. Phys. D: Appl. Phys. **37** (2004) 1289–1300 PII: S0022-3727(04)68968-6

Numerical investigation of interface region flows in mass spectrometers: neutral gas transport

Manish Jugroot[1], Clinton P T Groth[1,3], Bruce A Thomson[2], Vladimir Baranov[2] and Bruce A Collings[2]

[1] Institute for Aerospace Studies, University of Toronto, 4925 Dufferin Street, Toronto, Ontario, M3H 5T6, Canada

[2] MDS SCIEX, 71 Four Valley Drive, Concord, Ontario, L4K 4V8, Canada

E-mail: groth@utias.utoronto.ca

Received 15 September 2003
Published 31 March 2004
Online at stacks.iop.org/JPhysD/37/1289
DOI: 10.1088/0022-3727/37/8/019

Abstract

The supersonic jet flows of neutral gas from atmospheric to near-vacuum conditions in the interface region of mass-spectrometer systems is investigated by continuum-based (fluid) numerical simulations. An enhanced understanding of the neutral gas transport is of paramount importance to fully understand flows in the interface region of mass spectrometers, for it is the neutral dynamics that governs and drives the ions from the high pressure ion source through the interface orifice towards the ion optics and detector subsystems. The key features and structure of the complex neutral gas flow are examined and the influence of large pressure differences imposed across the interface region, orifice geometry, and gas skimmer configuration used for flow control are assessed. The flow structure is shown to be that of a classical under-expanded free jet for 'skimmer-absent' cases and very good agreement between the numerical predictions and empirical and experimental values is demonstrated. For the 'skimmer-present' cases, the shock structure downstream of the orifice and skimmer is identified and fully described and its influences on the flow skimming and focusing processes are discussed.

1. Introduction

Free jets and the often complex physical phenomena involved in rapid flow expansions are of interest in many technological applications including direct vapour deposition in materials and semiconductor processing, laser machining, rocket propulsion, and combustion [1–5]. Rapidly expanding and/or jet flows are also important in the operation of mass spectrometers, such as liquid chromatography (LC)/mass spectrometry (MS) systems used extensively in the trace analysis of biological fluids for drugs, metabolites, and natural biopolymers [6]. The LC/MS instruments make use of an atmospheric pressure ionization technique whereby sample ions are generated at atmospheric pressure from molecules that are contained in micro-droplets and the resulting ions are then transported from the atmospheric pressure conditions into a high vacuum system for spectroscopic analysis. As might be expected, the performance of these mass spectrometers is highly dependent on the neutral and ion gas transport from the ion source region to the mass detectors, and gaining an improved understanding of ion-source jet flows and related transport phenomena remains an active area of research.

This study is concerned with examining the rapidly expanding jet flows in the interface region of LC/MS systems situated beyond the ion source and before the ion optics, as depicted in the schematic diagram of figure 1. The important physical features of the expanding neutral gas flows downstream of the gas curtain orifice plate and gas

[3] Author to whom any correspondence should be addressed.

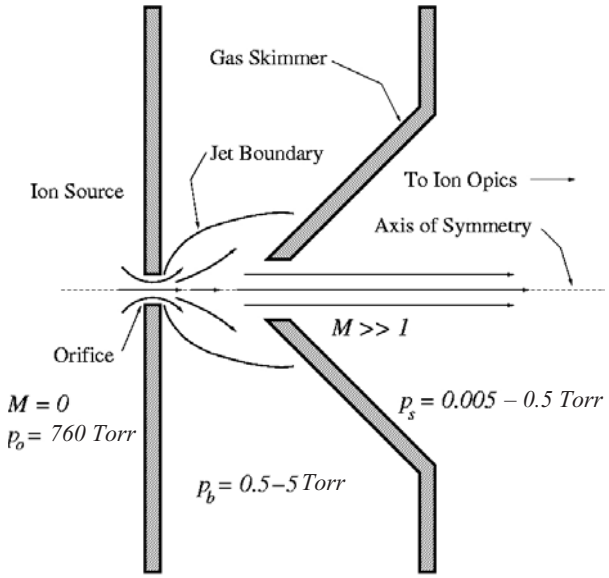

Figure 1. Schematic diagram of the interface region of the typical mass spectrometer systems showing orifice, neutral gas jet, gas skimmer, and typical operating pressures in each region of the flow.

skimmers are investigated using state-of-the-art computational fluid dynamics (CFD) analysis tools. Gas skimmers, in combination with applied electric fields, are used to control ion and neutral gas flows into the mass analyser. Key features of the neutral gas flows are examined and the influence of back-pressure, orifice geometry, and skimmer configuration are assessed. The primary objective of this study is to enhance the fundamental understanding of flows in the interface region of mass spectrometers. It is anticipated that this improved understanding will lead to the design of LC/MS systems with increased productivity and reduced testing times in the analysis of chemical compounds.

Companion numerical studies of ion transport in the interface regions of mass spectrometer systems have also been carried out recently by the authors. The non-equilibrium transport of ions through the background neutral gas under the influence of a prescribed electric field and subject to ion–neutral collision processes have been studied using an extended fluid model [7, 8]. As is the case for other technological devices [9, 10], the neutral gas is shown to play an important role in dictating the ion dynamics and cannot be neglected. The present neutral gas study, therefore, represents a vital and important first step towards an improved description of ion transport in the interface regions of mass spectrometers.

2. Governing equations for the neutral gas flows

It is assumed that the supersonic neutral gas flows in the interface regions of LC/MS mass spectrometers can be reasonably approximated as a near-thermal-equilibrium continuum. Similar continuum treatments of free jets and supersonic flows have been applied in previous research. See for instance the recent work by Klavuhn and McDaniel [4], Gribben *et al* [11], and Alvi *et al* [12]. In addition, the flows are assumed to be laminar (justifications for this assumption are provided in the discussion of the numerical results) and the thermal state of the neutral particles is determined by assuming that the gas is both a calorically and thermally perfect gas and obeys the ideal gas equation of state, $p = \rho RT$, where p is the static pressure, ρ the gas density, T the temperature, and R the gas constant. Accordingly, the conservation form of the partial differential equations governing the transport of the neutral gas are the well-known Navier–Stokes equations for a compressible fluid, which, using vector notation, can be expressed as

$$\frac{\partial \rho}{\partial t} + \nabla \cdot (\rho \boldsymbol{v}) = 0, \tag{1}$$

$$\frac{\partial}{\partial t}(\rho \boldsymbol{v}) + \nabla \cdot (\rho \boldsymbol{v}\boldsymbol{v} + p\boldsymbol{I} - \boldsymbol{\tau}) = \rho \boldsymbol{f}, \tag{2}$$

$$\frac{\partial}{\partial t}(\rho E) + \nabla \cdot \left[\rho \boldsymbol{v}\left(E + \frac{p}{\rho}\right) + \boldsymbol{q} - \boldsymbol{\tau} \cdot \boldsymbol{v}\right] = \rho \boldsymbol{f} \cdot \boldsymbol{v}, \tag{3}$$

where $\boldsymbol{v}$ is the velocity vector, $E = p/(\rho(\gamma - 1)) + |\boldsymbol{v}|^2/2$ is the specific total energy, $\boldsymbol{\tau}$ is a second-order tensor or dyadic quantity representing the viscous stresses with elements

$$\tau_{ij} = \mu\left(\frac{\partial v_i}{\partial x_j} + \frac{\partial v_j}{\partial x_i} - \delta_{ij}\frac{2}{3}\nabla \cdot \boldsymbol{v}\right), \tag{4}$$

$\boldsymbol{I}$ is the unit tensor, $\boldsymbol{q}$ the heat flux vector given by Fourier's Law, $\boldsymbol{q} = -\kappa \nabla T$, μ the dynamic viscosity, κ the thermal conductivity, and γ the specific heat ratio for the gas. The vector quantity $\boldsymbol{f}$ is the external body force per unit mass (acceleration) acting on the fluid. For this study, there are no additional body forces acting on the neutral gases. Furthermore, the physical geometry and flow fields of interest are axisymmetric [13–17]. Therefore, the two-dimensional axisymmetric form of the Navier–Stokes equations with $\boldsymbol{f} = 0$ is solved. Sutherland's Law is used to prescribe the viscosity.

The Knudsen number, $Kn = \lambda/\ell$, where λ is the particle mean free path and ℓ is the reference length scale (taken to be the orifice diameter, d_o, herein), can become relatively large in the high-Mach-number and low-pressure regions of the interface flows downstream of the orifice. Calculated values are in the range $0.01 < Kn < 0.4$ for the numerical solutions described below. This would imply that non-continuum and thermal non-equilibrium effects may be significant in these regions and that a continuum fluid dynamic model may not be strictly valid. Nevertheless, as a first step towards improving the understanding of interface flows in mass spectrometers, it is felt that a near-equilibrium continuum model is sufficiently accurate. It should be noted that non-continuum effects in high-speed expanding flows will primarily influence the thermal structure of the gas, but dynamic features such as velocity and density distributions and overall flow structure are not strongly affected [18–20]. Selezneva *et al* [20] report that continuum-based calculations for highly expanded supersonic jets may have errors in the total translational temperature of up to 30% in some cases. A full assessment of high-Knudsen-number non-equilibrium effects associated with spectrometer interface flows is currently being developed and will be the subject of future studies.

3. Numerical solution procedure

A commercial computational fluid dynamics flow solver (CFD++, developed by Metacomp Technologies) is used

to predict the high-speed expanding flows in the interface region of LC/MS systems. This flow solver employs an upwind total variation diminishing (TVD), finite-volume spatial discretization scheme in conjunction with a multigrid, accelerated, implicit time-marching procedure to solve the compressible axisymmetric form of the Navier–Stokes equations on an unstructured triangular mesh [21, 22]. A V-cycle and Gauss–Seidel smoother are employed in the multigrid convergence acceleration strategy. Clustering of the cells in the computational mesh is used to help to capture the important features of the complex jet flows downstream of the orifice. The CFD++ software has been carefully assessed and validated for a fairly comprehensive set of classical test cases including flow over cylinders, flat plates, compression ramps, and backward facing steps, as well as shear layer flow and injector flows [21, 22].

The commercial solver has parallel processing capabilities. The parallel implementation has been developed using the Message-Passing Interface (MPI) library [23] for performing inter-processor communications and the METIS graph partitioning software for performing a domain decomposition of the computational mesh [24]. Scalability has been tested on a Beowulf-class cluster consisting of 26 4-way Hewlett-Packard Alpha ES40 and ES45 SMP servers with 104 processors and 126 Gb of distributed memory; however, in most cases the neutral gas flow solutions were obtained using just two processors. For the interface flows considered here, the typical mesh size is 50 000 cells and a rather large number of iterations (about 20 000 iterations) is required for it to converge to a steady-state solution. Using two of the processors from the Beowulf cluster, the typical elapsed wall clock time for a calculation requiring about 19 CPU hours was 10 h.

4. Numerical results and discussion

4.1. Axisymmetric free-jet flow

Before proceeding to an investigation of interface flows with gas skimmers, expanding flows through orifices were investigated in the absence of gas skimmers. In this way, the flow expansion process downstream of the orifice could be first studied and better understood and the numerical model validated without the added complication of a skimmer.

When a high-pressure gas is exhausted through an orifice into a stagnant low-pressure chamber, the gas rapidly expands and results in the formation of an under-expanded free jet [13–16]. A schematic diagram of the under-expanded free jet is shown in figure 2. At the orifice, the flow is for the most part supersonic. The upstream high-pressure gas is, therefore, unaffected by the downstream flow conditions and the jet structure must adjust to match the back-pressure in the low-pressure chamber. The resulting free-jet flow is quite complex and characterized by thin non-isentropic regions (shocks) with large gradients in the properties of the gas. The key features of an under-expanded free jet include the: (i) barrel (intercepting) shock; (ii) jet boundary; (iii) triple point; (iv) Mach disc; and (v) reflected shock.

The free-jet expansion process can be understood as follows. Expansion waves form at the exit of the orifice/nozzle as the flow expands into the low-pressure chamber. The

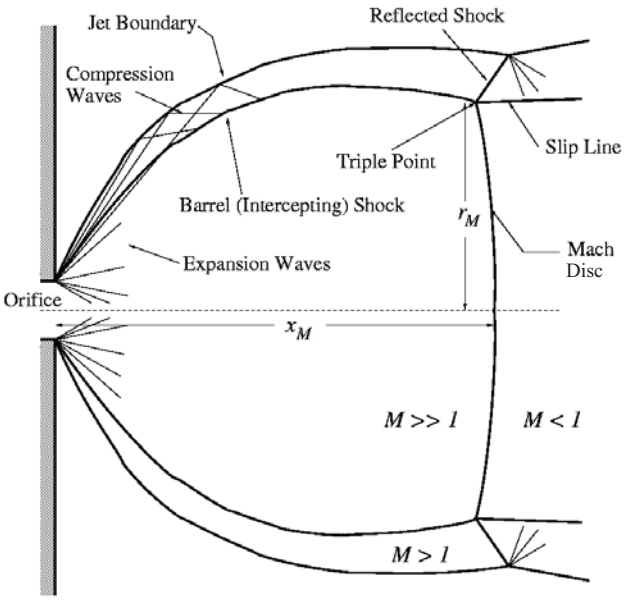

Figure 2. Schematic diagram of free jet flow shock structure.

expansion waves extend to the free-jet boundary and reflect as weak compression waves. The reflected compression waves coalesce to form the intercepting shock in the interior of the jet. Depending on the flow conditions, the intercepting shock may reflect regularly at the centreline or it may terminate in a triple-point Mach disc configuration (as in all the cases to be considered herein). The Mach disc is a slightly curved shock (the Mach disc is normal to the flow at the jet axis), behind which is a large region of subsonic flow bounded by a slipstream emanating from the triple point. The flow across the oblique intercepting shock remains supersonic but has a lower Mach number than the flow in the core of the jet. The flow downstream of the shock that reflects from the interaction of the intercepting shock and the Mach disc is also supersonic.

Numerical simulations of several under-expanded free jet flows were carried out using the flow solver described in section 3. The neutral gas was pure nitrogen. As a base case, the orifice diameter, d_o, was taken to be 0.75 mm; the upstream pressure, p_o, and temperature, T_o, were taken to be 760 Torr and 288 K, respectively, and the downstream pressure, p_b, was taken to be 0.5 Torr. The influences of the size of the orifice and downstream pressures were studied by varying both d_o and p_b. Numerical results were obtained for $d_o = 0.6$ and 0.25 mm and $p_b = 0.25$, 1, and 2 Torr. In addition, three different mesh sizes were used in the simulations (19 000, 41 000, and 84 000 cells) in order to study the effects of mesh resolution on solution quality and convergence. In all of the cases considered, no-slip boundary conditions were applied at all solid boundaries with a constant wall temperature $T = T_o$.

The numerical solution of the under-expanded free-jet flow of nitrogen for the base case using the 41 000-cell grid is shown in figure 3. The figure depicts the predicted flow streamlines and computed distributions of Mach number $M = |v|/a$ and entropy change $\Delta s = (R/(\gamma - 1))$ $\ln((p/p_o)/(\rho/\rho_\circ)^\gamma)$ [25], where a is the sound speed. The black coloured streamlines are associated with neutral gas flow that passes through the Mach disc whereas the white coloured

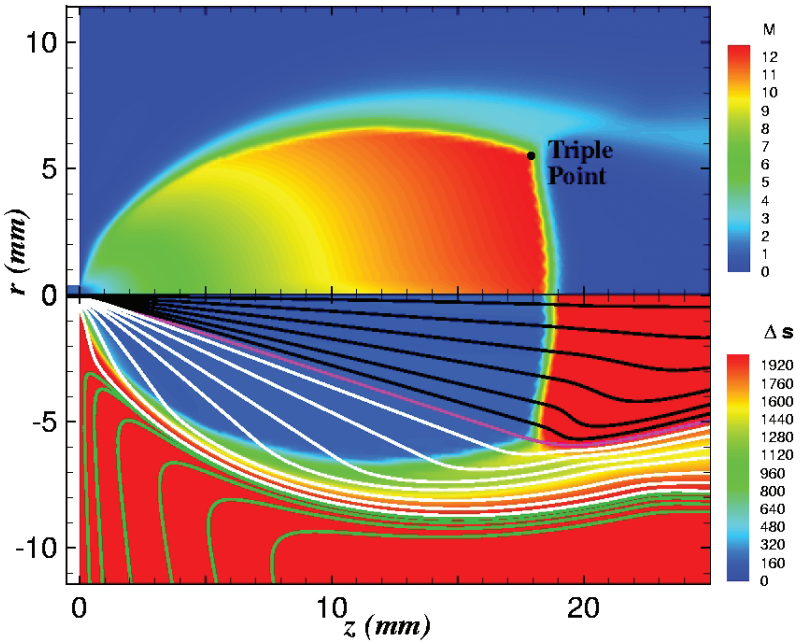

Figure 3. Computed flow streamlines and distributions of Mach number, M, and entropy change, Δs, for axisymmetric under-expanded free-jet flow with an orifice diameter of $d_o = 0.75$ mm and pressure ratio $p_o/p_b = 1520$. Results obtained using a 41 000 cell computational grid.

stream traces are associated with flow that passes through a region above the triple point via the intercepting shock. The purple coloured streamline marks the boundary between the flow passing through the Mach disc and flow passing above the triple point. The green coloured stream traces reflect the viscous entrainment of the low-pressure reservoir gas into the free jet flow that occurs in the mixing layer at the jet boundary. The flow is highly expanded downstream of the orifice. The pressure decreases by five orders in magnitude in the free jet and then increases abruptly again following the Mach disc to match the background pressure. The density and temperature also decrease and the flow speed increases monotonically. The Mach number exceeds 12 in the core region of the jet. The intercepting shock, jet boundary, triple point, Mach disc, and reflected shock are all quite evident in the predicted entropy and Mach number distributions and appear to be well resolved.

From the numerical solution for this case, it is estimated that the gas flow through the orifice, $\dot{m}$, the distance from the orifice to the position of the Mach disc, x_M, and diameter of the Mach disc, d_M, are $\dot{m} = 1.8 \times 10^{21}$ particles s^{-1}, $x_M = 19.1$ mm, and $d_M = 11$ mm, respectively. Ashkenas and Sherman [13] and French and Douglas [26, 27] provide some useful theoretical and empirical expressions for the gas flow through the orifice and location and diameter of the Mach disc that have been shown to agree quite well with available experimental data for a wide range of parameters. The gas flow through the orifice can be approximated by

$$\dot{m} = \frac{\pi}{4}\left(\frac{2}{\gamma+1}\right)^{(\gamma+1)/(2(\gamma-1))} n_o a_o d_o^2, \qquad (5)$$

where n_o and a_o are the number density and speed of sound in the high pressure reservoir, and the downstream location, and the diameter of the Mach disc can be estimated using

$$\frac{x_M}{d_o} = 0.67\sqrt{\frac{p_o}{p_b}}, \qquad \frac{d_M}{x_M} = \begin{cases} 0.42 & \text{for } \dfrac{p_o}{p_b} = 20, \\ 0.48 & \text{for } \dfrac{p_o}{p_b} = 10^3. \end{cases} \qquad (6)$$

For the base case, these expressions yield $\dot{m} = 2.1 \times 10^{21}$ particles s^{-1}, $x_M = 19.6$ mm, and $d_M = 9.4$ mm. It would seem that the numerical results are in relatively close agreement with the empirical results for the gas flow and dimensions of the free jet.

It is interesting to note that about 12% of the neutral particles within the free jet pass through the Mach disc, whereas most of the particles (88%) flow through a region upstream of the triple point via the intercepting shock as indicated by the calculated gas flow through sections A and B of figure 4. Furthermore, the calculated gas flows are somewhat higher downstream of the orifice than the computed value right at the exit of the orifice ($\dot{m} = 2.2 \times 10^{21}$ particles s^{-1} 14 mm downstream of the orifice). This increase in gas flow is due to viscous entrainment of low-pressure reservoir gas into the free-jet that occurs in the mixing layer at the jet boundary, as described by Ashkenas and Sherman [13]. Figure 3 illustrates the entrainment process. In general, the entrainment process and mixing layer growth at the free-jet boundary will have almost no effect on the flow inside the barrel shock, except for conditions of very low Reynolds numbers and very high pressure ratios.

Further validation of the numerical solution for this base case is provided by comparing the predicted results to measured data. An impact probe was used to obtain pressure measurements in a free jet that arises from the expansion of nitrogen gas from an atmospheric-pressure reservoir, through an orifice, into a low-pressure reservoir. The use of impact

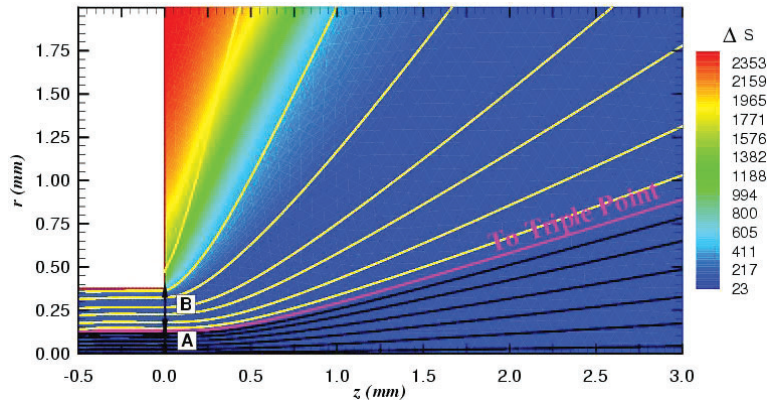

Figure 4. Computed flow streamlines emanating from the orifice for axisymmetric under-expanded free-jet flow with an orifice diameter of $d_o = 0.75$ mm, and pressure ratio $p_o/p_b = 1520$.

probes for performing pressure measurements in high speed flows is well established and described by Ashkenas and Sherman [13] and Rogers *et al* [28]. The 105.6 mm long stainless steel tubular probe was manufactured with a 1 mm inside diameter and a 1.62 mm outside diameter. A McAllister XYZ MB2004 Manipulator was used to control and position the impact probe in the jet downstream of the orifice and a laser light source was used to aid in orienting the probe with respect to the flow axis of symmetry. The orifice geometry and pressure ratio, p_o/p_b, were identical to those of the base case. Detailed surveys of the axial and radial profiles of the pressure were obtained. For near continuum flows, an impact probe operates much like a pitot probe and provides measurements of the stagnation pressure, p_o, which can be related to the static pressure, p, by following expression:

$$\frac{p_o}{p} = \begin{cases} \left[1 + \dfrac{\gamma - 1}{2} M^2\right]^{\gamma/(\gamma-1)} & \text{for } M \leqslant 1, \\ \dfrac{\gamma+1}{2} M^2 \left[\dfrac{((\gamma+1)/2)M^2}{(2\gamma/(\gamma+1))M^2 - ((\gamma-1)/(\gamma+1))}\right]^{1/(\gamma-1)} & \text{for } M > 1. \end{cases} \tag{7}$$

In the case of supersonic flow ($M > 1$), the measured pitot pressure corresponds to the post-shock stagnation pressure behind a detached bow shock that forms at the leading edge of the probe.

Results of the comparisons between measured and predicted pitot pressures for the base free-jet flow case are given in figures 5(*a*)–(*c*). The figure depicts computed and measured radial profiles of the pressure at distances of 13.97, 17.78, and 22.23 mm downstream of the orifice. The first two stations correspond to locations upstream of the Mach disc and the last station is located downstream of the Mach disc. It can be seen that the experimental data are not quite symmetrical about $r = 0$ due to slight asymmetries in the experimental jet and uncertainties in the location of the axis of symmetry. The three profiles all have the same general topology. There is a pressure plateau in the core region of the jet, followed by a sharp increase in the stagnation pressure across the barrel shock, and finally a decrease in pressure to match the background value of 0.5 Torr. Although, there is some disagreement between measured and predicted values of

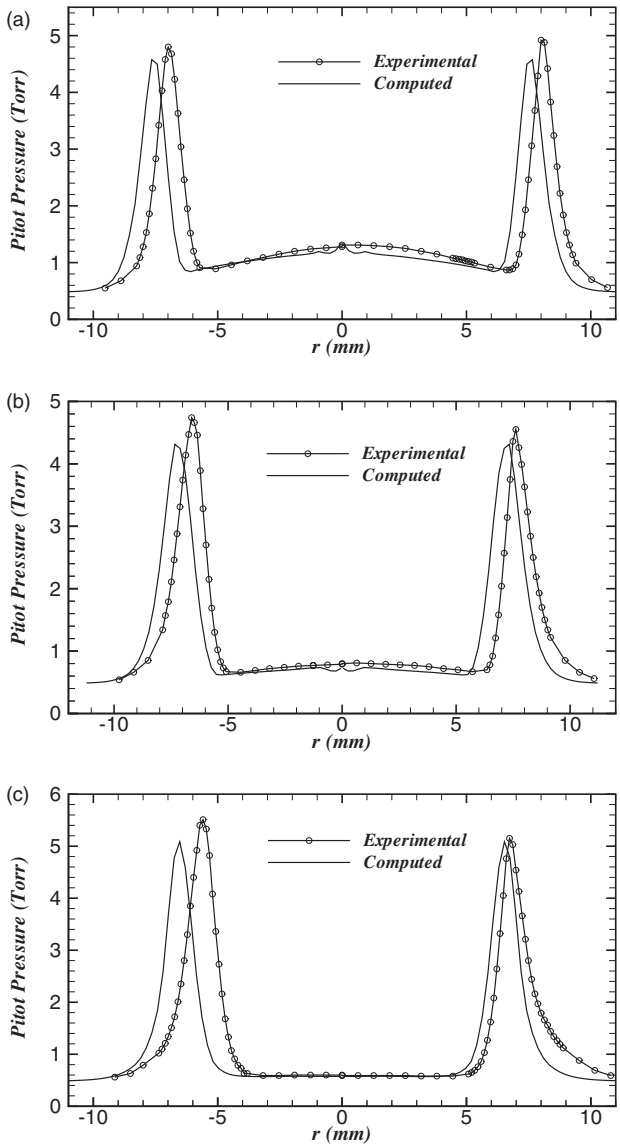

Figure 5. Comparison of computed and measured radial pitot probe pressure profiles 13.97 mm (*a*), 17.78 mm (*b*), and 22.23 mm (*c*) downstream from the orifice for axisymmetric under-expanded free-jet flow with an orifice diameter $d_o = 0.75$ mm and pressure ratio $p_o/p_b = 1520$.

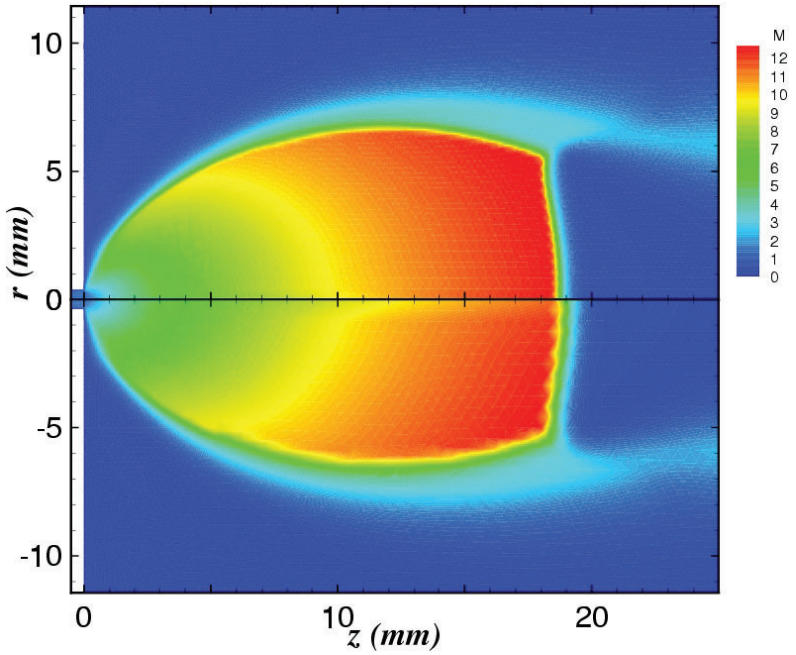

Figure 6. Computed distributions of Mach number, M for axisymmetric under-expanded free-jet flow with an orifice diameter of $d_o = 0.75$ mm and pressure ratio $p_o/p_b = 1520$. A comparison of results for the 84 000 cell (top panel) and 19 000 cell (bottom panel) computational grids is shown.

the pitot pressure close to the orifice (this difference is most likely due to probe interference effects), overall the agreement between the experimental data and numerical results is very good, providing strong support for the validity and reliability of the calculations. In particular, the excellent agreement in the pressure profiles shown in figures 5(*a*)–(*c*) would imply that the boundaries and extent of the free jet are well predicted by the flow solver and, moreover, that the assumption that the flow is laminar is justified. Although the Reynolds number, based on the orifice diameter and flow conditions at the orifice throat, was calculated to be in the range of 8000–12 000, the length of the orifice is less than one diameter ($\approx$0.9 d_o) and hence the boundary layers in this region are thin and not fully developed and there is insufficient distance for the flow to transition and become fully turbulent within the jet. Downstream of the orifice, the Reynolds number drops to values of about 800 just upstream of the Mach disc and has values in the range of 2–10 downstream of the Mach disc. Even if small regions of the downstream jet flow are locally turbulent, the assumption that the flow is fully turbulent would not be justified. Moreover, Reynolds-averaged Navier–Stokes calculations of the free-jet flow, performed by the authors but not shown here, based on the assumption that the flow is fully turbulent and using the standard two-equation k–ϵ model for turbulence [29] deviate from empirical and experimental data by a large amount.

Figure 6 shows a direct comparison of the predicted Mach number distributions for the base free-jet flow case obtained using the 84 000 and 19 000 cell computational grids. Comparing these results with the Mach number distribution of figure 3 for the 41 000 cell mesh provides a good indication of the convergence of the numerical solution as the mesh is refined. It can be seen that the free-jet solution is well represented on the 41 000 cell mesh and that this solution does not change significantly when going to the finer, 84 000 cell mesh. In fact it appears that all three mesh resolutions (19 000, 41 000, and 84 000 cells) are sufficient to capture the key features of the expansion process.

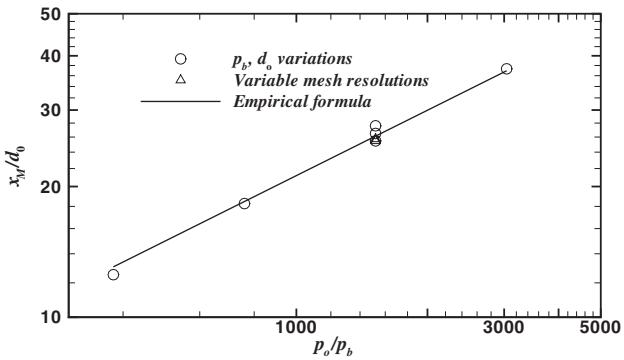

Figure 7. Location of the Mach disc as a function of the pressure ratio.

Finally, the results of varying the orifice diameter, background pressure, and mesh resolution on the structure of the free jet are summarized in figure 7, which shows the variation in the location of the Mach disc as a function of pressure ratio for $d_o = 0.75$, 0.6, and 0.25 mm and $p_b = 0.25$, 0.50, 1, and 2 Torr. The dependence of the numerical solution on refinement of the computational mesh is also depicted for the 19 000, 41 000, and 84 000 cell computational grids. In addition, the curve corresponding to the empirical expression of equation (6) is given. The general structures of the computed free jets for these cases are very similar to that of the base case and detailed results are, therefore, not shown. It can be seen from the results shown in figure 7 that the computed dimensions of the Mach disc as a function of back-pressure and orifice diameter agree very well with the empirical correlation.

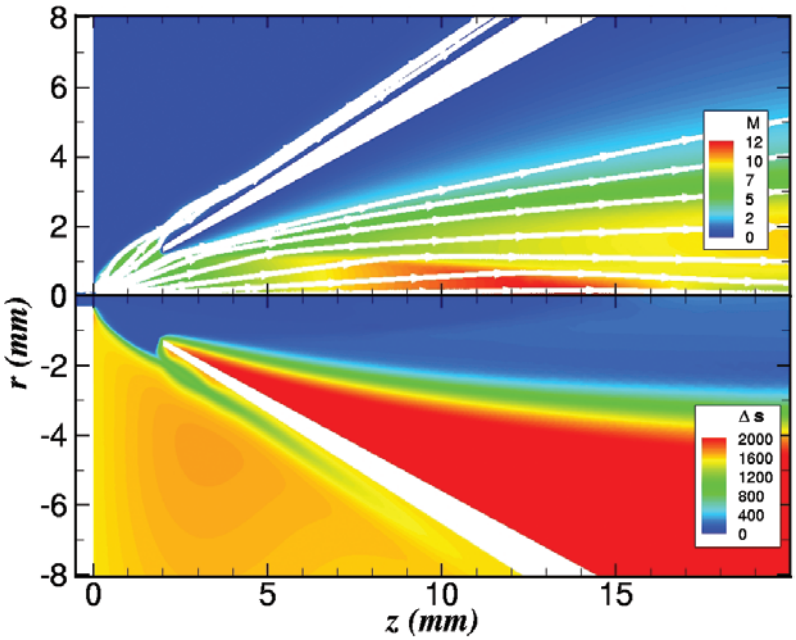

Figure 8. Computed flow streamlines and distributions of Mach number, M, and entropy change, Δs, for axisymmetric supersonic jet flow with an orifice diameter of $d_o = 0.6$ mm, a pressure ratio $p_o/p_b = 225.5$, a skimmer back-pressure of $p_s = 0.055$ Torr, and a conical skimmer with diameter $d_s = 2.5$ mm and cone angle $\alpha_s = 60^\circ$. The orifice-to-skimmer distance, x_s, is 2 mm.

Moreover, as previously indicated by the results of figures 3 and 6, a mesh independent result is obtained using 41 000 cells, at least in terms of the overall jet structure. The predicted values of x_M/d_o for the 19 000 and 41 000 cell cases are about 25.73 and 25.47, respectively, which corresponds to a difference of less than 1%. The difference between the predicted locations of the Mach disc for the 41 000 and 84 000 cell meshes is even less and essentially negligible.

4.2. Axisymmetric jet with gas skimmer

Expanding neutral flows in the presence of gas skimmers are now considered. Gas skimmers, as shown in figure 1, are introduced in the interface regions of mass spectrometer systems to reduce the flux of neutral gas to the ion optics and to focus ions that are being transported by the neutral flow. Supersonic-jet/skimmer configurations have been the subject of previous, mostly experimental, research efforts related to molecular beams [17, 26, 30]. Here, we seek to assess by numerical methods the impact of an axisymmetric conical-shaped skimmer with skimmer orifice diameter of $d_s = 2.5$ mm and a cone angle of $\alpha_s = 60^\circ$ on the structure of the supersonic jets emanating from orifices of diameters $d_o = 0.6$ and 0.75 mm. The range of pressures of interest here are generally higher than those encountered in molecular beam studies. For the first set of cases considered, differential pumping is used such that the back-pressure between the orifice and the skimmer, p_b, is maintained at 3.37 Torr for the $d_o = 0.6$ mm case ($p_b = 4.7$ Torr for the $d_o = 0.75$ mm case) and the back-pressure downstream of the skimmer, p_s, is lower and has a value of 0.055 Torr for the $d_o = 0.6$ mm case ($p_s = 0.183$ Torr for the $d_o = 0.75$ mm case). Air was used as the working gas in each of these first set of cases, to enable comparison with measured pitot pressure data, which were obtained only for air flows in the skimmer geometries.

Figure 8 shows the axisymmetric jet flow solution for the gas skimmer case with $d_o = 0.6$ mm, $p_o/p_b = 225.5$, $d_s = 2.5$ mm, $\alpha_s = 60^\circ$, and $x_s = 2$ mm. A 48 000-cell mesh was used to obtain the solution. A systematic mesh refinement study indicated that this level of mesh resolution was sufficient to obtain solution accuracies similar to that obtained for the free-jet cases. Note that mesh stretching was used to cluster computational cells near the leading edge and inner surface of the skimmer.

As for the free-jet cases, the distributions of Mach number and entropy change are shown in the figure, along with the computed streamlines. From the figure, it should be evident that the overall structure of the flow with a gas skimmer is quite different from that of the free jet. A schematic diagram of the skimmer jet flow structure that has been inferred from the results of this study is given in figure 9. The presence of the skimmer prevents the jet of air from fully expanding and, as a consequence, a Mach disc does not form. Unlike in the free-jet case, the neutral gas remains highly supersonic in the core of the jet far downstream of the orifice and skimmer. The flow velocity is also higher in the core with the skimmer present due to a reduced flow cross section. The skimmer not only confines the jet expansion process but also serves to divide the neutral flow, diverting a significant portion of the flow. Approximately 70% of the neutral particles pass through the skimmer in this case (30% are diverted). The leading edge of the skimmer is immersed in the on-coming supersonic jet flow and this leads to the formation of a leading edge (bow) shock. The topology of the inner portion of this skimmer shock is that of an inverted cone with an apex located approximately 20 mm downstream of the orifice. The skimmer shock deflects the radially directed neutral flow in the jet core, turning it back towards the axis of symmetry, and resulting in an axially directed flow. The apex of the shock surface corresponds to the location where the skimmer shock reflects from the axis

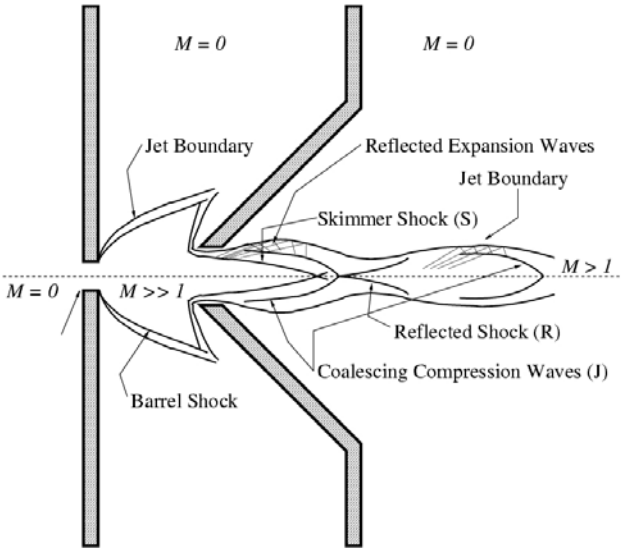

Figure 9. Schematic diagram of skimmer jet flow shock structure showing the skimmer shock (S); the coalescing reflected compression waves from the jet boundary (J); the reflected shock (R); and the succession of expansion/re-compression cells.

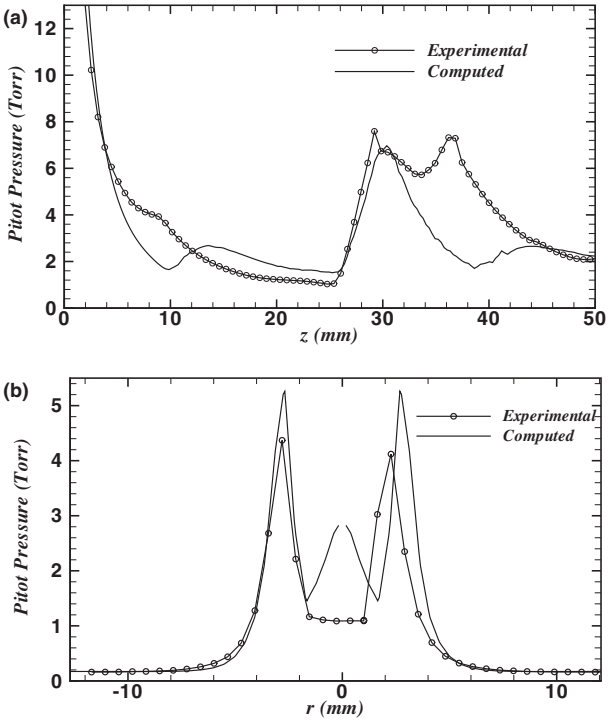

Figure 10. Comparison of computed and measured axial pitot pressure profiles (*a*) and radial pitot pressure profiles 25.4 mm downstream from the orifice (*b*) for axisymmetric supersonic jet flow with an orifice diameter of $d_o = 0.75$ mm, a pressure ratio $p_o/p_b = 161.7$, a skimmer back-pressure of $p_s = 0.183$ Torr, and a conical skimmer with diameter $d_s = 2.5$ mm and cone angle $\alpha_s = 60^\circ$. The orifice-to-skimmer distance, x_s, is 2 mm.

of symmetry. Note that the general structure of the skimmer shock is also clearly visible in the results of figures 15(*a*)–(*d*), which show computed distributions of the neutral gas pressure for a different set of flow conditions and a different working gas. A detailed discussion of these results is given later in this subsection.

A numerical solution for the supersonic jet with skimmer flow for $d_o = 0.75$ mm, $p_o/p_b = 161.7$, $d_s = 2.5$ mm, $\alpha_s = 60^\circ$, and $x_s = 2$ mm was also determined using a 48 000-cell computational grid, and the results are very similar to those described earlier. Impact probe measurements of the flow pressure were made for this second case and provide further validation of the numerical predictions. Figures 10(*a*) and (*b*) show comparisons of the measured and computed pitot pressures. The axial distribution of the pitot pressure and the radial distribution of the pressure 25.4 mm downstream of the orifice are both given. Overall, the agreement between the experimental results and numerical predictions is reasonably good. Discrepancies in the results may be attributed to probe interference effects, uncertainties in the probe location, and asymmetries in the actual experimental flow field.

Figure 11 illustrates the effect of the skimmer location on the structure of the resulting jet flow. Computed distributions of entropy change are shown for orifice-to-skimmer distances of $x_s = 2$ mm and $x_s = 3$ mm, respectively. Moving the skimmer away from the orifice generally places the leading edge of the skimmer further into the core of the expanding jet flow and leads to increased flow diversion and reduced flow through the skimmer. Placing the gas skimmer nearer the orifice has the reverse effect. These results also show that the location of skimmer shock on the axis depends directly on the position of the tip of the skimmer.

A more complete understanding of the influences of skimmer location and back-pressure on the jet flow and shock structure is provided by the additional numerical results given in figures 12–15. For the cases considered hereafter, nitrogen is the working gas and differential pumping is used such that the back-pressure between the orifice and the skimmer, p_b, is maintained at 0.5 Torr ($p_o/p_b = 1520$) and the back-pressure downstream of the skimmer, p_s, is generally lower and has values ranging from 0.005 to 0.5 Torr. The orifice diameter is $d_o = 0.75$ mm and a conical skimmer with diameter $d_s = 3$ mm and cone angle $\alpha_s = 60^\circ$ is considered.

Figure 12 shows the distribution of entropy for supersonic jets in nitrogen for two different back-pressure values. The location of the skimmer shock on the axis is exactly the same for both values of the pressure. It can be concluded from these results that the location of the reflection of the skimmer shock on the axis of symmetry (the apex of the inverted skimmer shock cone) does not depend on the background pressure and only depends on the position of the tip of the skimmer in the flow. This feature is really a consequence of the uniformity of the governing parameters in the core of the free jet as depicted in figure 13, showing the radial variation of the Mach number for three different pressure ratios ($p_o/p_b = 760$, $p_o/p_b = 1520$, and $p_o/p_b = 3040$). It is quite evident that the value of the Mach number near the axis is essentially the same for all three cases and grows uniformly with increasing radius until the outer boundary of the jet is encountered, indicated by a sharp decrease in the Mach number to the zero value of the stationary background gas. When the skimmer tip is situated close to the axis of symmetry (i.e. for small values of the radius, r), the skimming process is initiated at approximately the same flow Mach number as shown in figure 13 and is, therefore, independent of the background pressure.

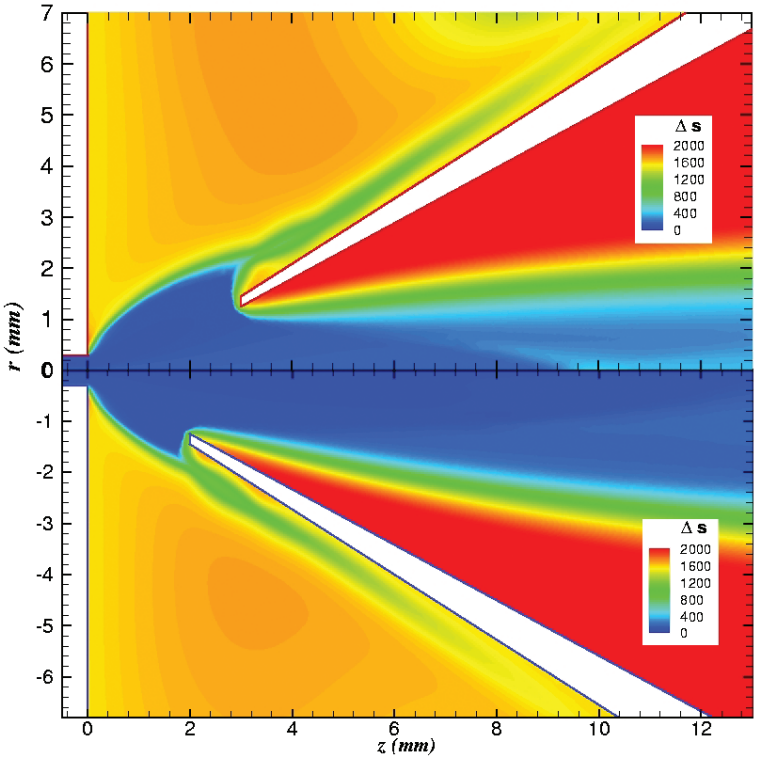

Figure 11. Computed distributions of entropy change, Δs, for axisymmetric supersonic jet flows with an orifice diameter of $d_o = 0.6$ mm, a pressure ratio $p_o/p_b = 225.5$, a skimmer back-pressure of $p_s = 0.055$ Torr, and a conical skimmer with diameter $d_s = 2.5$ mm and cone angle $\alpha_s = 60^\circ$. A comparison of the shock structure for orifice-to-skimmer distances of $x_s = 2$ mm (bottom panel) and $x_s = 3$ mm (top panel) is shown.

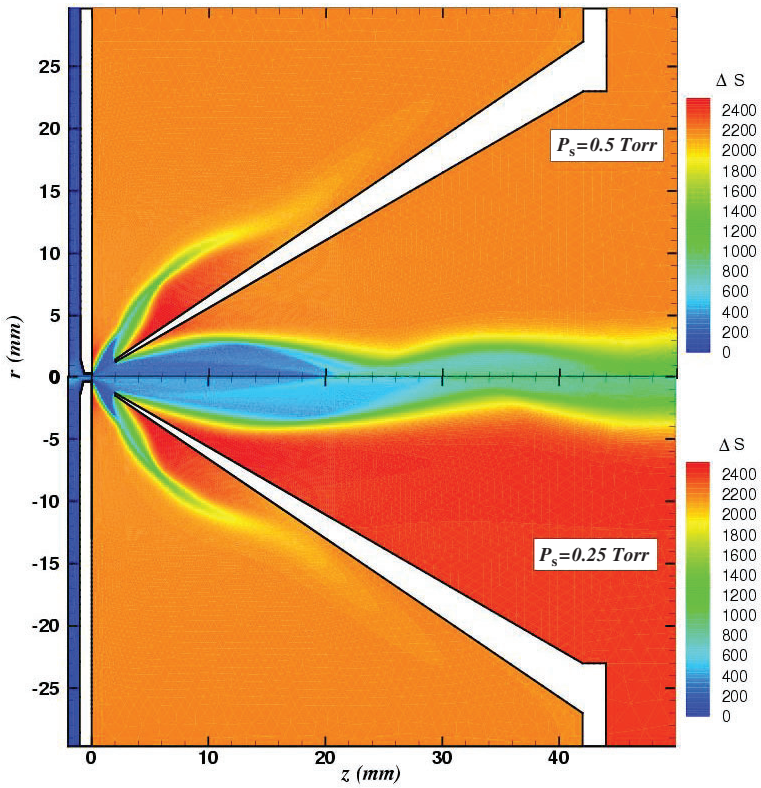

Figure 12. Computed distributions of entropy change, Δs, for axisymmetric supersonic jet flows with an orifice diameter $d_o = 0.75$ mm, a pressure ratio $p_o/p_b = 1520$, and a conical skimmer with diameter $d_s = 3$ mm and cone angle $\alpha_s = 60^\circ$. A comparison of the shock structure for the two skimmer back-pressures $p_s = 0.25$ Torr, (bottom panel) and $p_s = 0.5$ Torr (top panel) is shown.

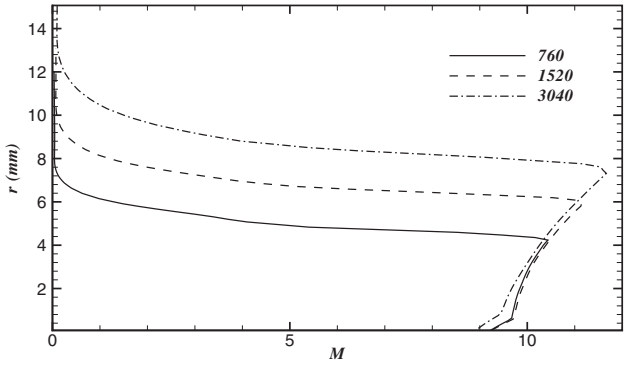

Figure 13. Computed radial distributions of Mach number in the core of the free-jet for pressure ratios $p_o/p_b = 760$, $p_o/p_b = 1520$, and $p_o/p_b = 3040$.

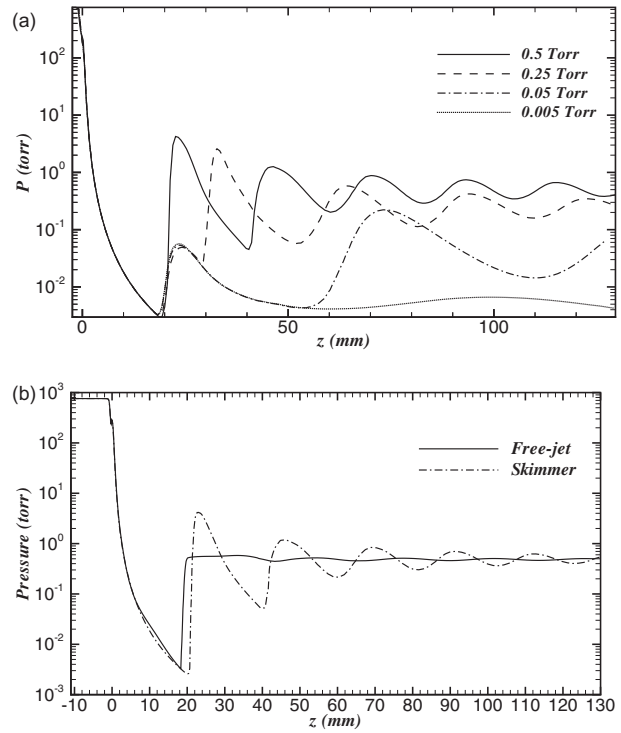

Figure 14. Computed distributions of pressure on the axis of symmetry for a pressure ratio $p_o/p_b = 1520$. Distributions for skimmer back-pressures $p_s = 0.5$, $p_s = 0.25$, $p_s = 0.05$, and $p_s = 0.005$ Torr are compared in (*a*) and the distribution for the skimmer configuration with $p_s = 0.5$ Torr is compared with the free-jet result in (*b*).

However, if the first skimmer shock structure is independent of the background pressure, this is clearly not the case for the subsequent shock cells downstream of the skimmer, as depicted in figure 12. Figure 14(*a*) shows the axial distribution of the static pressure in the skimmer jet for four different skimmer background pressures ($p_s = 0.5$, $p_s = 0.25$, $p_s = 0.05$, and $p_s = 0.005$ Torr). Ahead of the reflection point for the skimmer shock, all of the pressure distributions are coincident; however, downstream of the reflection point, very different features are observed, depending on the background pressure. These differences will now be discussed.

It is interesting to first point out the differences introduced by the skimmer compared to the free-jet case.

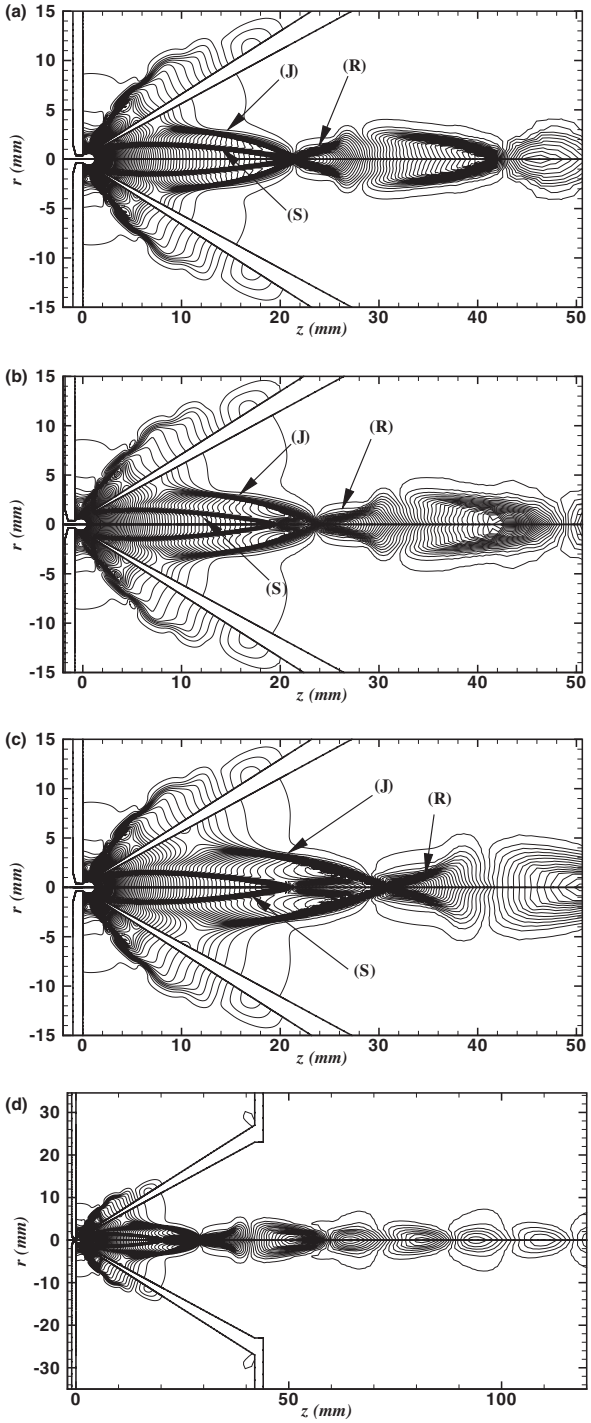

Figure 15. Computed pressure contours showing expansion/re-compression plume structure downstream of skimmer, for $p_s = 0.5$ Torr (*a*), $p_s = 0.375$ Torr (*b*), and $p_s = 0.25$ Torr (*c*), and $p_s = 0.25$ Torr (*d*). The orifice diameter is $d_o = 0.75$ mm, the pressure ratio is $p_o/p_b = 1520$, and a conical skimmer with diameter $d_s = 3$ mm and cone angle $\alpha_s = 60^\circ$ is used. (S) denotes the skimmer shock; (J) the coalescing reflected compression waves from the jet boundary; and (R) the reflected shock.

Figure 14(*b*) depicts the predicted pressure along the axis of symmetry for a 0.75 mm orifice jet flow in nitrogen (the pressure ratio across the orifice is $p_o/p_b = 1520$). In the skimmer-present case, upstream of the first shock

reflection, the neutral gas undergoes a significant over-expansion process. The reflected shock re-compresses the flow again. Following this primary re-compression process downstream of the skimmer, the neutral gas then undergoes a sequence of secondary (weaker) expansion processes followed by secondary re-compression processes. This expansion/re-compression pattern is repeated many times downstream of the skimmer, as can be observed in the pressure plot of figure 14(*b*). The expansion/re-compression features are also present for the free-jet case, but are very weak in magnitude and are, therefore, barely detectable for the pressure ratios that are considered here. The free-jet flow is subjected to a strong re-compression process through the Mach disc and then weak expansion cells are observed downstream of the skimmer orifice. Clearly, the presence of the skimmer amplifies the expansion/re-compression effects by reducing the cross-sectional area available to the jet flow.

The expansion/re-compression pattern or plume structure downstream of the skimmer indicated by the results of figure 14 exhibit a complex wave structure. They result in several maxima and minima in the axial pressure distribution. As noted above, the downstream plume structure has some similarities with the sequential shock cell patterns observed in under-expanded free jets [11]. However, the overall flow structure is quite different due to the presence of the skimmer. The skimmer prevents the flow from expanding freely, concentrating the flow near the axis. As a result, the Mach number remains very high in the core of the primarily axially-directed flow downstream of the skimmer.

Figures 15(*a*)–(*c*) show the computed pressure profiles for three skimmer back-pressures: $p_s = 0.5$ Torr, $p_s = 0.375$ Torr, and $p_s = 0.25$ Torr, respectively. The pressure ratio across the orifice is again $p_o/p_b = 1520$ for these cases. All three results clearly illustrate the characteristic expansion/re-compression cell pattern of the flow downstream of the reflected skimmer shock for the low pressure regimes that are of interest here. From these pressure field plots the essential features of the plume structure can be ascertained. The first or primary expansion/re-compression cell is composed of two structures. The first structure is the skimmer shock (S) described previously and represented by the inverted shock cone. The computed skimmer shocks are identical for all three pressure ratios. The reflection of the skimmer shocks from the axis of symmetry can also be identified in the figures. The second clearly evident feature of the primary expansion/re-compression cell is a surrounding structure (J) corresponding to an axisymmetric oblique shock wave resulting from coalescing compression waves formed from the reflection of rarefaction waves from the jet boundary. The core jet flow downstream of (J) is turned towards the axis of symmetry by the shock (i.e. the shock compresses the flow). This axisymmetric oblique shock also intersects the axis of symmetry and is reflected as another oblique shock. This reflected shock is identified as shock (R) in figures 15(*a*)–(*d*). The reflected shock (R) subsequently undergoes a change in curvature and is reflected as expansion waves from the jet boundary. Note that the core flow in the jet is turned towards the jet boundary by the reflected processes resulting in flow expansion, which initiates another expansion/re-compression cell with expansion waves that again reflect from the jet boundary. The phenomenon is repeated again and again until the plume structure gradually decays as the pressures in the jet and stationary background gas equilibrate and viscous effects and mixing become predominant far downstream. An enlarged view of the complete flow structure and computational domain for the $p_s = 0.25$ Torr case is shown in figure 15(*d*), where multiple expansion/re-compression cells are observed downstream of the skimmer. The schematic diagram of figure 9 highlights the essential features of the flow structure downstream of the skimmer showing the primary shock structures (S) and (J) followed by the succession of secondary expansion/re-compression cells of decreasing intensity containing (R).

It should be noted that the coincidence of (J) and (S) on the axis of symmetry shown in figure 15(*a*) is completely fortuitous as confirmed by the results for the other pressure ratios given in figures 15(*b*) and (*c*). In fact, as opposed to the skimmer shock, the location and radial extent of (J) depends on the background pressure downstream of the skimmer. Lowering the background pressure shifts the oblique shock (J) further downstream.

5. Conclusions

The important physical features of axisymmetric under-expanded free jets and supersonic jets with gas skimmers have been examined using continuum-based numerical simulations. The complex structure associated with these expanding flows appears to be well reproduced in the simulations, and the numerical predictions are shown to be in good agreement with both experimental data and available empirical results. The structure of the flow downstream of the orifice and skimmer have been identified and discussed. The presence of the skimmer leads to clear differences compared to the free-jet and the flow remains supersonic in the core of the jet downstream of the orifice and skimmer. Several shock structures have been identified downstream of the skimmer and have been shown to be dependent on the background pressure. Understanding the different parameters controlling the flow structure helps in optimizing the skimming process at the tip of the skimmer and focusing of the neutral gas (and thus the ion beam) beyond the interface region of mass spectrometer systems.

Acknowledgments

This research was supported by the Natural Sciences and Engineering Research Council of Canada (NSERC CRD Grant 254794-01). Funding for the parallel computing facility used to perform the numerical simulations described herein was obtained from the Canadian Foundation for Innovation and Ontario Innovation Trust (CFI Project No 2169). The authors are very grateful to these funding agencies for this support.

References

[1] Groves J F and Wadley H N G 1997 *Composites* **28** (part B) 57
[2] Alvi F S and Iyer K G 1999 AIAA Paper 99-1829 *5th AIAA/CEAS Aeroacoustics Conf. and Exhibit (Bellevue, WA)*

[3] Kim J U, Clemens N T and Varghese P L 1999 AIAA Paper 99-0452 *37th AIAA Aerospace Sciences Meeting and Exhibit (Reno, NV)*
[4] Klavuhn K G and McDaniel J C 2001 *J. Propulsion Power* **17** 1067
[5] Chen K, Yao Y L and Modi V 1998 *J. Manuf. Sci. Eng.* **122** 429
[6] Thomas R 2001 *Spectroscopy* **16** 28
[7] Jugroot M, Groth C P T, Thomson B A, Baranov V and Collings B A 2003 AIAA Paper 2003-4210 *36th AIAA Thermophysics Conf. (Orlando, FL)*
[8] Jugroot M, Groth C P T, Thomson B A, Baranov V and Collings B A 2004 *J. Phys. D: Appl. Phys.* **37** 550
[9] Jugroot M and Harvey J K 2001 *Aeronaut. J.* **105** 613
[10] Jugroot M, Bayle P, Yousfi M and Eichwald O 1999 *J. Phys. D: Appl. Phys.* **32** 106
[11] Gribben B J, Badcock K J and Richards B E 2000 *AIAA J.* **38** 275
[12] Alvi F S, Ladd J A and Bower W W 2002 *AIAA J.* **40** 599
[13] Ashkenas H and Sherman F S 1966 *Rarefied Gas Dynamics* (New York: Academic) p 84
[14] Crist S, Sherman P M and Glass D R 1966 *AIAA J.* **4** 68
[15] Abbet M 1971 *AIAA J.* **9** 512
[16] Adamson T C and Nicholls J A 1959 *J. Aero/Space Sci.* **26** 16
[17] Campargue R 1984 *J. Phys. Chem.* **88** 4466
[18] Anderson J B, Andres R P, Fenn J B and Maise G 1966 *Rarefied Gas Dynamics* (New York: Academic) p 106
[19] Mukherjee J, Gantayet L M and Ahmad S A 2000 *J. Phys. D: Appl. Phys.* **33** 1386
[20] Selezneva S E, Boulos M I, van de Sanden M C, Engeln R and Schram D C 2002 *J. Phys. D: Appl. Phys.* **35** 1362
[21] Peroomian O, Chakravarthy S and Goldberg U C 1997 AIAA Paper 97-0724 *35th AIAA Aerospace Sciences Meeting and Exhibit (Reno, NV)*
[22] Peroomian O, Chakravarthy S and Goldberg U C 1998 AIAA Paper 98-0116 *36th AIAA Aerospace Sciences Meeting and Exhibit (Reno, NV)*
[23] Gropp W, Lusk E and Skjellum A 1999 *Using MPI* (Cambridge, MA: MIT Press)
[24] Karypis G and Kumar V 1998 *J. Parallel Dist. Comput.* **48** 96
[25] Zucrow M J and Hoffman J D 1976 *Gas Dynamics* vol 1 (New York: Wiley)
[26] French J B 1970 *CASI Trans.* **3** 77
[27] Douglas D J and French J B 1988 *J. Anal. At. Spectrom.* **3** 743
[28] Rogers K W, Wainwright J B and Touryan K J 1966 *Rarefied Gas Dynamics* (New York: Academic) p 151
[29] Wilcox D C 2002 *Turbulence Modeling for CFD* (La Cañada, CA: DCW Industries)
[30] Beijerinck H, Gerwen R V, Kerstel E, Martens J, Vliembergen E V, Smits M and Kaashoek G 1985 *J. Chem. Phys.* **96** 153